Geohazard Mechanics 4 (2026) 10–20

Contents lists available at ScienceDirect

Geohazard Mechanics

journal homepage: www.keaipublishing.com/en/journals/geohazard-mechanics

Effects of excavation geometry in energy evolution in underground mines

Linnea Lundvall[a], Niklas Burvall[a], Zongze Li[a,*], Wenjun Luo[a], Jinyang Fan[b], Minghe Ju[c,d], Yang Zou[a,**]

[a] Division of Mining and Geotechnical Engineering, Luleå University of Technology, Luleå, 97187, Sweden
[b] State Key Laboratory of Coal Mine Disaster Dynamics and Control, School of Resources and Safety Engineering, Chongqing University, Chongqing, 400044, China
[c] State Key Laboratory of Intelligent Construction and Healthy Operation & Maintenance of Deep Underground Engineering, China University of Mining and Technology, Xuzhou, 221116, China
[d] School of Mechanics and Civil Engineering, China University of Mining and Technology, Xuzhou, 221116, China

ARTICLE INFO

Keywords:
Excavation geometry
Energy evolution
Underground mines
Rockburst

ABSTRACT

With mines reaching into greater depth, problems with violent failures become more prevalent, such as rockbursts. To assess the potential for such occurrences, understanding energy dynamics is crucial. This study delves into the impact of excavation shape, aspect ratios, inclined angles and in-situ stress on dissipated plastic energy and released kinetic energy through numerical simulations. Detailed analyses of plastic zone around rectangular and elliptical excavations, varying in aspect ratios, unveiled the distinct patterns of tensile and shear plastic zone. Quantitative assessments of dissipated plastic energy and released kinetic energy highlighted contrasting behaviors between rectangular and elliptical excavations across various aspect ratios. Although the relationships between these energies and excavation parameters are found to be intricate, it becomes evident that: with an increase in the aspect ratio, both shear and tensile plastic zones exhibit a growing trend, and their distribution shows a high degree of consistency with regions of energy concentration. When the aspect ratio is below 1.5, elliptical excavations release slightly less kinetic energy than rectangular ones. Beyond 1.5, this relationship reverses. Moreover, upon exploring inclined angles, critical angles were identified, delineating points where the influence of aspect ratio nearly diminishes. Under the given in-situ stress conditions, approximately 50° and 20° serve as the critical angles for dissipated plastic energy and released kinetic energy, respectively. Changes in the degree of in-situ stress anisotropy have a limited impact on the overall energy trends but significantly alter the critical values of aspect ratio and inclination angle. When the in-situ stress ratio matches the excavation aspect ratio, both forms of energy reach their minimum values. These findings illuminate the complex interplay between excavation geometry and energy dissipation, offering invaluable insights for designing effective excavations and devising strategies to mitigate failures.

1. Introduction

As mining operations extend deeper underground, the risk of violent failures, such as rockbursts, becomes increasingly significant (Fig. 1) [1,2]. These sudden, explosive failures result from the rapid release of accumulated strain energy under high-stress conditions, posing severe threats to underground infrastructure, equipment, and, most critically, worker safety [3–5]. Rockbursts are particularly prevalent in deep mining environments where high in-situ stresses lead to stress redistribution and energy concentration around excavation boundaries [6,7]. Understanding the factors influencing the occurrence and intensity of such events is crucial for improving excavation design and ensuring the stability of underground structures [8–10]. Among these factors, excavation geometry plays a fundamental role in stress redistribution and energy storage [11–13]. However, despite extensive research on stress-induced failures in underground mining, a notable gap remains in comprehensively understanding how excavation shape influences energy changes, particularly in relation to kinetic energy release and plastic strain work, both of which are closely associated with rockburst potential.

* Corresponding author.
** Corresponding author.
E-mail addresses: zongze.li@associated.ltu.se (Z. Li), yang.zou@ltu.se (Y. Zou).
Peer review under the responsibility of Liaoning University.

https://doi.org/10.1016/j.ghm.2026.01.001
Received 13 March 2025; Received in revised form 29 May 2025; Accepted 3 January 2026
Available online 6 January 2026

(a) China (b) Canada

Fig. 1. Schematic diagram of rockburst in deep mine from China and Canada.

Theoretical analyses have provided valuable insights into stress redistribution around underground openings [14]. Early solutions were largely based on elastic constitutive models and focused primarily on circular openings, as these geometries allow for simplified analytical solutions [15]. The classic Kirsch equations, for instance, describe the stress field around a circular opening in an elastic medium, serving as a fundamental reference for excavation stability assessment [16–18]. However, real-world underground excavations rarely conform to such idealized geometries. Many mining operations employ non-circular designs, including elliptical, rectangular, or irregularly shaped openings, due to engineering constraints, geological conditions, or optimization requirements [19]. These more complex geometries induce heterogeneous stress concentrations, making it challenging to apply traditional analytical models [20]. Furthermore, as excavation-induced deformations extend into the plastic domain, theoretical solutions become increasingly difficult to derive. In deep mining environments, plastic deformation is a critical factor, as rock masses often experience significant inelastic behavior before failure [21–23]. In such cases, theoretical approaches based solely on elastic assumptions become insufficient, necessitating alternative methods to investigate the stress-energy response of excavations.

Numerical simulations have emerged as a powerful tool for addressing these complexities [24]. By incorporating advanced constitutive models and accounting for plastic deformation, numerical modeling techniques such as the finite element method (FEM) and discrete element method (DEM) provide detailed insights into stress redistribution, failure evolution, and energy dynamics around excavations [25,26]. These methods enable the study of dynamic failure mechanisms, which are difficult to capture through purely theoretical approaches. One of the most critical aspects of excavation-induced energy evolution is the relationship between kinetic energy release and total plastic strain work [27,28]. The kinetic energy released during failure events serves as a direct indicator of rockburst intensity, reflecting the potential for sudden energy bursts that could lead to catastrophic failures [29,30]. Meanwhile, plastic strain work represents the energy dissipated through deformation, providing insight into how stress is absorbed and redistributed within the rock mass [31,32]. A deeper understanding of how excavation shape influences these energy components is essential for improving underground stability assessments and optimizing excavation designs to mitigate failure risks.

Despite the importance of excavation geometry in underground mining stability, relatively few studies have systematically explored its influence on energy distribution and failure mechanisms [33,34]. While previous research has examined stress redistribution patterns associated with different excavation shapes, the direct link between excavation-induced stress changes and energy transformation remains insufficiently understood [35,36]. Most studies evaluating excavation stability have relied on traditional stress criteria, which focus on localized stress concentrations but fail to capture the full energy evolution process [37]. Given the increasing reliance on energy-based failure prediction models, there is a pressing need to bridge this gap by systematically evaluating the effects of excavation geometry on energy redistribution, kinetic energy release, and plastic strain work [38]. Understanding these interactions is critical for improving rockburst prediction and optimizing excavation strategies to enhance both safety and operational efficiency.

The objective of this study is to investigate the effects of excavation geometry on energy evolution in underground mining environments. Using numerical simulations, different excavation shapes will be modeled to analyze stress redistribution patterns and quantify their impact on energy storage and release mechanisms. Specifically, this study aims to determine how excavation shape influences the magnitude and spatial distribution of kinetic energy release and plastic strain work, both of which are fundamental to assessing rockburst potential. By employing advanced simulation techniques, this research will provide quantitative insights into the energy-related consequences of excavation design, helping to refine energy-based failure assessment models. Furthermore, the findings will contribute to the optimization of excavation geometries, ultimately improving the stability and safety of underground mining operations. The results of this study will serve as a foundation for developing improved excavation strategies that minimize energy accumulation in high-stress environments, thereby reducing the likelihood of sudden failure events.

2. Energy balance

The overall energy balance can be described in relation to the released energy (W_r), defined as the difference between the work done at the boundary of the model and the total stored and dissipated strain energies. These equations are taken from *Energy Calculation Chapter* in 3DEC manual and is supported by Salamon [15].

$$W_r = W - \left(U_c + U_b + W_j + W_p\right) \tag{1}$$

where W_r is the released energy; W is the total boundary loading work supplied to the system; U_c is the total stored strain energy in material; U_b is the total change in potential energy of the system; W_j is the total dissipated energy in joint shear; and W_p is the total dissipated work in plastic deformation of intact rock.

Based on energy balance, the released energy can also be calculated according to the kinetic energy mass damping work, the work performed at viscous boundaries and the strain energy in excavated material:

$$W_r = U_k + W_d + W_v + U_m \tag{2}$$

where U_k is the current value of kinetic energy in the system; W_d is the total work dissipated by mass damping; W_v is the work done by viscous boundaries; and U_m is the total strain energy in excavated material.

The total plastic strain work plays a key factor in determining the optimal shape for excavation in geotechnical conditions due to its per-

manent deformations. The plastic work is determined by calculating the difference between the total strain energy and the elastic energy component:

$$\Delta W_p = \Delta W_T - \Delta W_e \tag{3}$$

Total dissipated plastic strain work is the sum of ΔW_p for all blocks at each timestep.

Understanding the total mass damping work is essential for assessing the dissipated violent failure energy. To ascertain this, it's necessary to calculate the kinetic energy:

$$U_k = \sum_{i=1}^{ngp} \frac{1}{2} m_i (\dot{u}_i)^2 \tag{4}$$

where U_k is the current value of kinetic energy in the system (kinetic energy of all gridpoints in a given timestep); m_i is the mass of gridpoint I; and $\dot{u}_i$ is the velocity at gridpoint i.

The damped energy (W_k) can be simplified version of the equation of motion:

$$\frac{\partial \dot{u}}{\partial t} = \frac{\sum F}{m} - \alpha\, \dot{u} \tag{5}$$

where $\dot{u}$ is the velocity of a gridpoint of mass, m; $\sum F$ is the force sum at the gridpoint; and α is the damping coefficient.

The damping force is determined by:

$$F_d = m\, \alpha\, \dot{u} \tag{6}$$

Rate of damped energy change at a gridpoint is calculated as:

$$\dot{W_d} = F_d\, \dot{u} = m\, \alpha \dot{u}^2 \tag{7}$$

The damped energy over a timestep at a gridpoint, j is determined by:

$$W_{dj} = \int \alpha\, m\, \dot{u}^2\, dt = 2\alpha\, \Delta t\, U_{kj} \tag{8}$$

where W_{dj} is the energy damped at gridpoint j; and U_{kj} is the kinetic energy of the gridpoint j.

Total mass damping work is the sum of all gridpoints and timesteps:

$$W_d = \sum_{i=1}^{nt} \sum_{j=1}^{ngp} W_{dj} \tag{9}$$

where W_d is the total energy damped; nt is the number of timesteps; and ngp is the number of gridpoints.

In static calculations, once the system reaches its final equilibrium state, the bulk of the kinetic energy gets absorbed by mass damping, thereby transforming into damping energy. Consequently, the total released kinetic energy can be computed as follows:

$$W_{rk} = U_k + W_d \tag{10}$$

The meanings of different energy symbols are listed in Table 1.

Table 1
The meanings of different energy symbols.

Energy symbol	Meaning
W_r	Released energy
W	Total boundary loading work supplied to the system
U_c	Total stored strain energy in material
U_b	Total change in potential energy of the system
W_j	Total dissipated energy in joint shear
W_p	Total dissipated work in plastic deformation of intact rock
U_k	Current value of kinetic energy in the system
W_d	Total work dissipated by mass damping
W_v	Work done by viscous boundaries
U_m	Total strain energy in excavated material
ΔW_p	Changes in dissipated plastic energy at each timestep
ΔW_T	Changes in strain energy at each timestep
ΔW_e	Changes in elastic energy at each timestep
W_k	Damped energy
W_{dj}	Energy damped at gridpoint j
U_{kj}	Kinetic energy of the gridpoint j
W_d	Total energy damped
W_{rk}	Total released kinetic energy

3. Verification of numerical modeling

3.1. Energy calculation

It is essential to demonstrate that the energy calculation in numerical simulation agrees with relevant theoretical results. Salamon deduced the energy components associated with an increase from R_0 to R_1 in the radii of a cylindrical tunnel:

$$\frac{W_{rk}}{U_m} = \frac{1 - (R_0/R_1)^2}{1 - 2\gamma + (R_0/R_1)^2} = \beta \tag{11}$$

$$\frac{W}{U_m} = 2(1+\beta), \frac{U_c}{U_m} = 2 + \beta, \frac{W_r}{U_m} = 1 + \beta \tag{12}$$

where γ is Poisson's ratio.

A numerical simulation was carried out to analyze energy variations as a circular opening originally sized at $R_0 = 0.5$ m is enlarged to different radii R_1 under an elastic model. The simulation considered a Young's modulus of 15 GPa and a Poisson's ratio of 0.25. Fig. 2 illustrates the comparison between theoretical predictions and numerical findings, revealing remarkable alignment between the two. This alignment underscores the efficacy of the energy computation method employed in the simulation.

It's worth noting that the relationships among different energy components only depend on the Poisson's ratio and the excavation size under elastic models. However, the introduction of plastic deformation in the model would render these relationships intricate. They would then rely not only on the Poisson's ratio and excavation dimensions but also on in-situ stress and the other mechanical properties. Consequently, further investigation through numerical simulation is imperative to comprehend these complexities.

3.2. Brittle failure simulation

The intensity of violent failure in underground excavations largely depends on the brittleness of the rock mass. Traditional continuum models using failure criteria like Hoek–Brown or Mohr–Coulomb often fail to accurately capture brittle failure behavior, as they assume simultaneous mobilization of cohesion and friction. To address this,

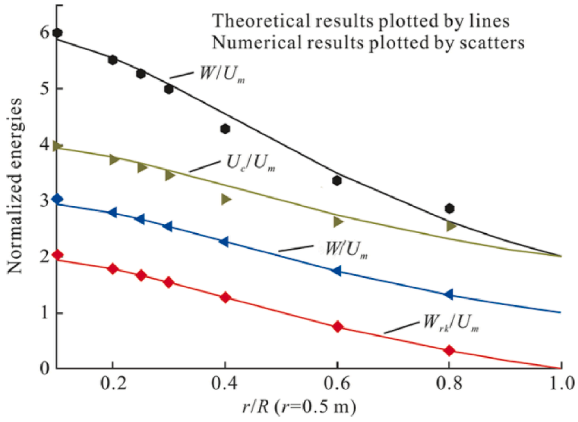

Fig. 2. Normalized energy changes due to an increase in the radius of a circular tunnel from R_0 to R_1.

Hajiabdolmajid et al. [39] proposed the cohesion weakening and friction strengthening (CWFS) model, which better represents brittle rock behavior by incorporating progressive cohesion loss due to tensile cracking and delayed mobilization of frictional strength with plastic strain as illustrated in Fig. 3 [36].

In low confinement environments, such delay is a defining feature of brittle failure, where extensile cracking dominates. The CWFS model was implemented to simulate the shaft excavation at Atomic Energy of Canada Limited's Underground Research Laboratory (URL), using the mechanical parameters listed in Table 2. The shaft, with a radius of 1.75 m, is subjected to an in-situ stress field of $\sigma_1 = 60$, $\sigma_2 = 45$ and $\sigma_3 = 11$ MPa. The failed and plastic zone observed in field and obtained through numerical simulation are shown in Fig. 4, respectively.

Numerical simulations using the CWFS model successfully reproduced the field-observed failure patterns, showing V-shaped notches in high compressive stress zones and shear-dominated failure, along with limited tensile failure along the direction of maximum principal stress. The depth of the plastic zone in simulation (2.45 m) closely matches field data (2.28 m), with minor discrepancy due to mesh size. This agreement validates the model's effectiveness in capturing the essential characteristics of brittle failure, forming the basis for subsequent analyses.

3.3. Model setup

The stress redistribution was demonstrated to be affected by the excavation geometry including both the excavation shape, aspect ratio and the inclination of the excavation concerning the direction of principal stress [40]. To further investigate its effects on the energy evolutions, numerical models were established based on the same geological conditions as presented in section 3.2 and varying excavations shapes including circular, elliptical, and rectangular shapes. To facilitate comparison, the areas of various shapes are made to be equal, and this can be computed using Eq. (13).

$$A = \pi \cdot r^2 = \pi \cdot a \cdot b = L_1 \cdot L_2 \tag{13}$$

where r is the radius of circular excavation which is fixed to be 1.75 m; a and b are the semi axes of the elliptical excavation; and L_1 and L_2 are side length of the rectangular excavation. As shown in Fig. 5, a and L_1 are parallel to the maximum principal stress, while b and L_2 are parallel to the minimum principal stress.

Scenarios with varying aspect ratios of the elliptical and rectangular excavations expressed in Eq. (14) were simulated. It's worth noting that a circular excavation represents a special case among elliptical excavations, occurring when the aspect ratio equals 1.

$$R_{as} = b/a = L_2/L_1 \tag{14}$$

In practical scenarios, the long or short axes of non-circular excavations typically do not align with the principal stress. Hence, the study also delved into examining the impact of the inclination angle (β) between the long axis of elliptical openings and the maximum principal stress, as depicted in Fig. 6.

4. Effects of excavation geometry

4.1. Effects of shape

The plastic zone around the rectangular and elliptical excavations with different aspect ratios R_{as} are presented in Figs. 7 and 8, respectively. Shear failure and tension failure are plotted in red and green colour, respectively.

It can be found that due to stress relief, the tensile plastic zone adjacent to rectangular excavations are prominently situated along the left and right walls, perpendicular to the maximum principal stress. Conversely, shear plastic zone manifest on the other two walls, notably concentrated at the corners due to compressive stress concentration. Concurrently, the areas of these plastic zone expand with an increasing aspect ratio. The pattern of plastic zone surrounding elliptical excavations closely resembles that of rectangular excavations. However, a subtle distinction lies in the concentration of shear plastic zone—within the midsections of the upper and lower walls for elliptical excavations, as opposed to the corners for rectangular ones.

Quantifying the volume of plastic zones provides a more precise understanding of how excavation geometry influences plastic deformation. Table 3 presents the volumes of shear, tensile, and total plastic zones for elliptical and rectangular excavations across various aspect ratios. Fig. 9 illustrates the evolution of these volumes with changing aspect ratio. As shown in Fig. 9, both shear and tensile plastic zone volumes generally increase with aspect ratio for both excavation shapes, though the growth trends differ. When the aspect ratio (R_{as}) is less than 4.0, the plastic zone volume induced by elliptical excavation is generally smaller than that of rectangular excavation. Shear plastic zones are generally smaller than tensile zones, with the latter showing a more pronounced increase. In elliptical excavations, the shear plastic zone stabilizes at an aspect ratio of 0.75, while in rectangular excavations, stabilization occurs beyond an aspect ratio of 1.5. Notably, at $R_{as} = 4.0$, the plastic zone volume for elliptical excavation exceeds that of the rectangular case, deviating from the previous trend. This anomaly may be attributed to the elliptical opening at $R_{as} = 4.0$ behaving like a narrow crack. When oriented perpendicular to the maximum principal stress, stress concentration at the crack tips significantly enlarges the plastic zone, as detailed in Fig. 10.

To investigate the relationship between stress concentration and plastic zone development, the numerical simulation results for $R_{as} = 4.0$ are selected for detailed analysis, as shown in Fig. 10. Fig. 10b and c

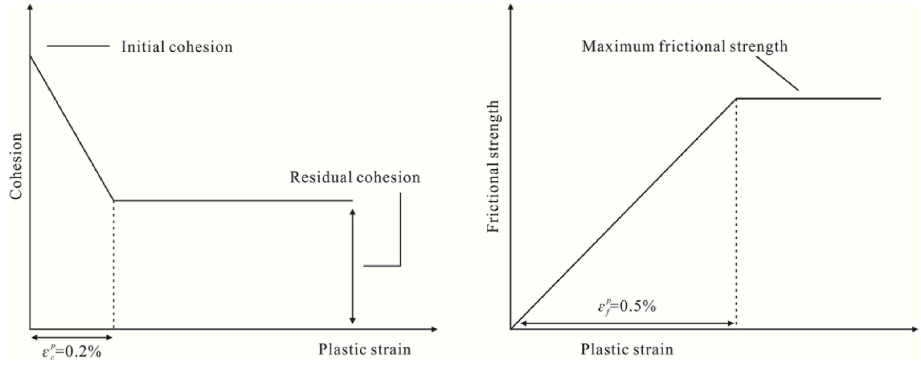

Fig. 3. Illustration of the cohesion-loss and frictional strength mobilization as a function of plastic strain.

Table 2
Mechanical properties in numerical models.

Item	Cohesion	Friction angle	Dilation angle	Tensile strength	Young's modulus	Poisson's ratio	Density
Initial	60 GPa	0°	0°	10 MPa	50 MPa	0.2	2630 kg/m^3
Residual	15 GPa	48°	30°				
Plastic strain	0.2 %	0.5 %	0.5 %				

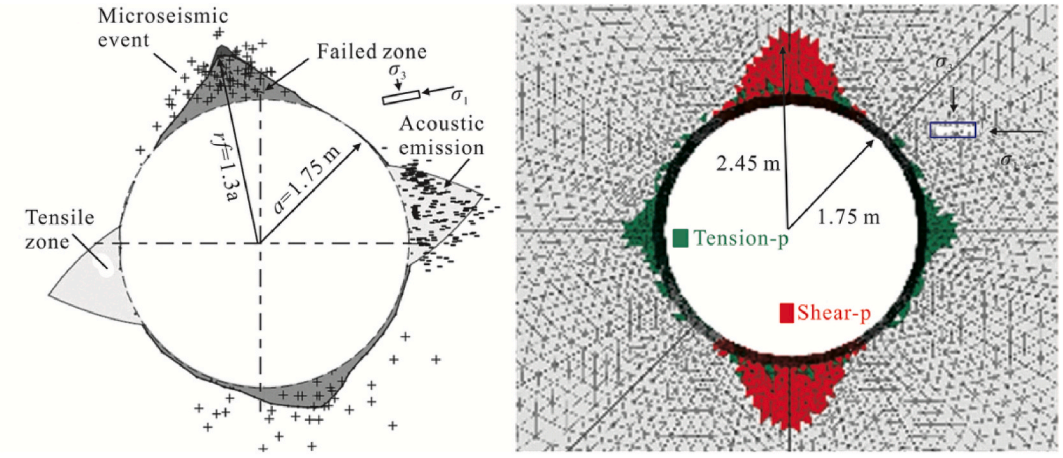

(a) Shape of the failed zone observed around the circular test tunnel [39]

(b) Plastic zones in numerical model

Fig. 4. Damage zone in field test and numerical model.

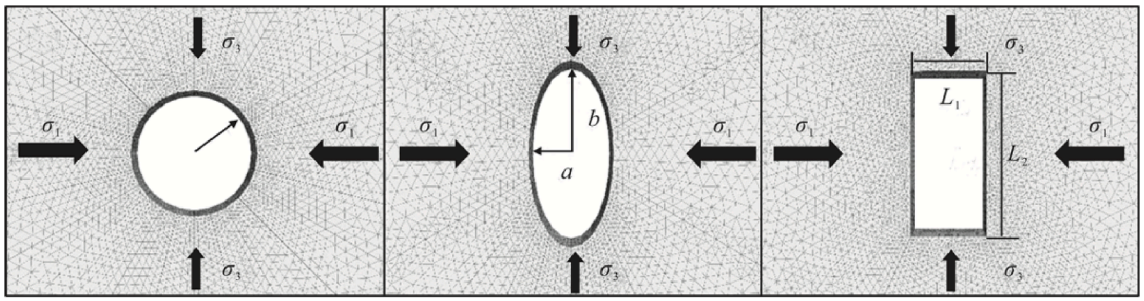

(a) Circular excavation (b) Elliptical excavation (c) Rectangular excavation

Fig. 5. Excavation with different shapes.

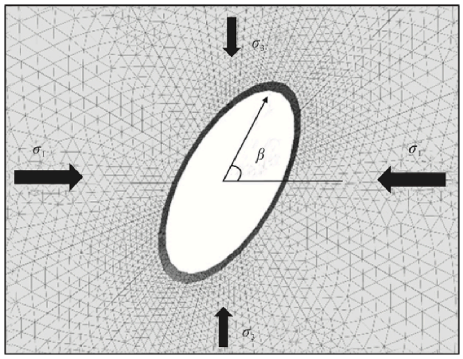

Fig. 6. Elliptical excavation with different inclination angles.

displays the distributions of maximum and minimum principal stresses for the rectangular excavation. It is worth noting that: due to software settings, compressive stress is negative and tensile stress is positive. For clarity, regions with compressive stress greater than 8×10^7 Pa and tensile stress less than 5×10^6 Pa are shown in white. It is evident that, for the rectangular excavation, compressive stress peaks at the longitudinal ends, as indicated by the yellow dashed boxes, corresponding to the red shear plastic zone in Fig. 10a. Maximum tensile stress appears along the lateral sides and at the four corners, aligning with the green tensile failure regions in Fig. 10a. Fig. 10e and f shows the compressive and tensile stress distributions for the elliptical excavation. Similarly, the highest compressive stresses occur at the longitudinal ends, as indicated by the purple dashed boxes, while tensile stresses concentrate at the midpoints of the lateral sides and along the diagonals. This consistency between stress concentration zones and plastic zone distribution confirms the reliability of the numerical simulation.

To quantitatively compare the plastic failed degree, the dissipated plastic energy was employed, and the outcomes are presented in Fig. 11a.

The dissipated plastic energies associated with both rectangular and

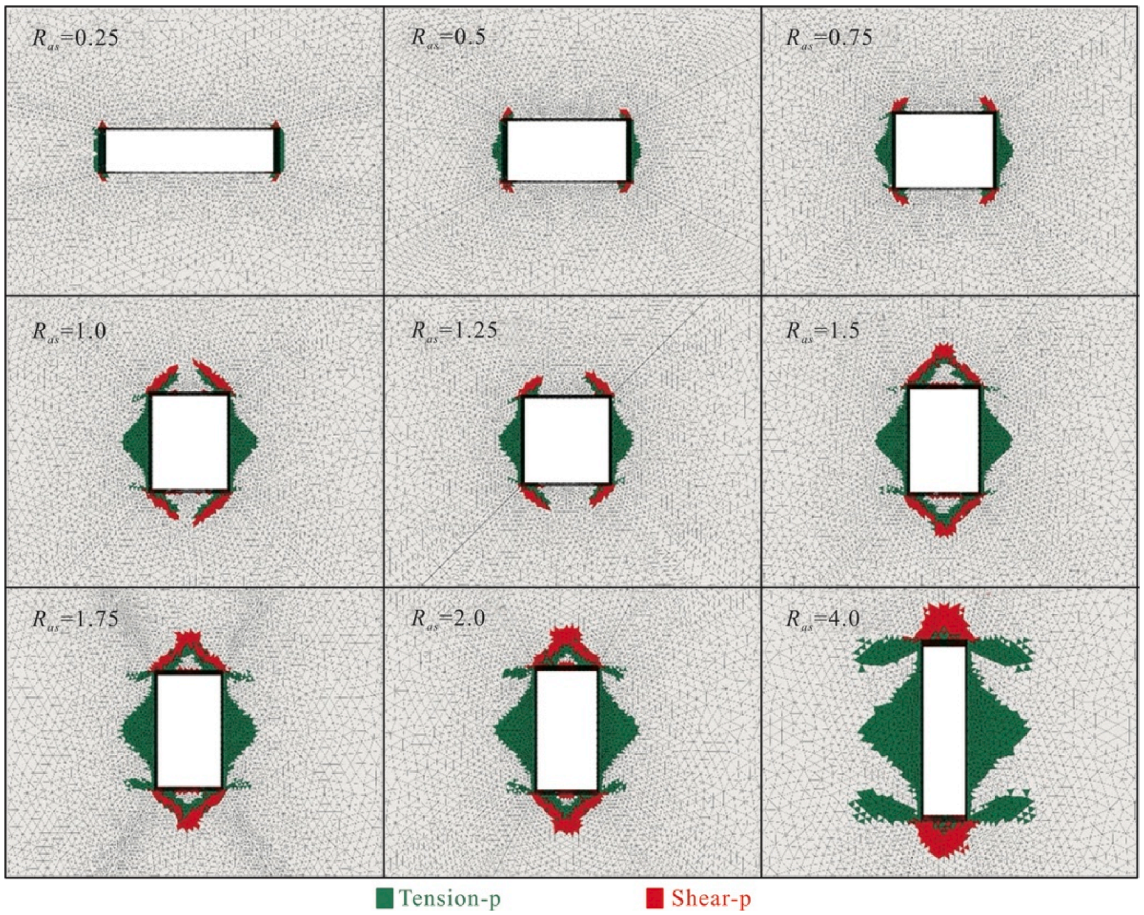

Fig. 7. Plastic zone of rectangular excavations with different aspect ratios.

elliptical excavations exhibit an increasing trend with rising aspect ratios. However, they have uneven pace of growth. The curve slopes exhibit distinct behaviours: for rectangular excavations, the increase in dissipated plastic energy can be bifurcated into two stages, delineated by the critical aspect ratio of 1.5. Beyond this threshold, the growth rate becomes smaller. In contrast, the dissipated plastic energy linked to elliptical excavations undergoes three stages. Initially, there is rapid growth when the aspect ratio is below 1.0, followed by a nearly constant phase within the range of 1.0–2.5. Remarkably, within this range, the dissipated energy remains lower than that observed in rectangular excavations. However, as the aspect ratio exceeds 2.5, a sharp escalation transpires, surpassing even the energy dissipation observed in rectangular excavations when it is larger than 3.5. This escalation correlates with extensive shear stress concentration occurring at the upper and lower ends of the ellipse, equivalent to crack tips.

The findings suggest using the strategic control measures to manage plastic failure degrees. Specifically, minimizing the length of excavations within the tensile stress concentration zone is advisable to mitigate failure scale. Conversely, ensuring an adequate length of excavations within the shear stress concentration zone is crucial to prevent extensive shear stress concentration akin to crack tips. Considering the relationship between the zones of tensile and shear concentration alongside in-situ stress orientations, it becomes evident that reducing the aspect ratio, manifested as a shorter length perpendicular to the maximum principal stress and a longer length parallel to the minimum principal stress, is a viable strategy to regulate dissipated plastic energy.

From Fig. 11b, it can be found that the released kinetic energies are nearly the same under rectangular and elliptical excavations and both linearly increase with an increase in aspect ratio. Specifically, when the aspect ratio remains below 1.5, the released kinetic energy attributed to elliptical excavations is marginally lower than that linked to rectangular excavations. However, beyond an aspect ratio of 1.5, a shift occurs in their relative magnitudes.

Analysis of Fig. 11 underscores a crucial point: the relationships governing dissipated plastic energy and released kinetic energy do not align. Thus, designing an aspect ratio to minimize plastic deformation does not inherently translate to a reduction in the kinetic energy induced by excavation. It becomes imperative to distinctly consider these divergent energy aspects. Additionally, it's evident that a universal conclusion regarding the superior shape is untenable as the performance of various shapes varies across different aspect ratios. Optimizing excavation geometry necessitates a comprehensive approach encompassing both the choice of shape and its specific aspect ratio. Broadly, excavations aligning their longer axis with the maximum principal stress exhibit superior performance in preserving shape and managing induced dynamic disturbances. This underscores the significance of considering both shape and aspect ratio when striving for optimal excavation design.

4.2. *Effects of inclined angle*

Fig. 12 shows the plastic zone of elliptical excavations with aspect ratio 1.5 under different inclined angles. There are not notable alterations in the area of shear plastic zone, and the V-shaped notches consistently maintain their orientation perpendicular to the maximum principal stress, unaffected by shifts in the orientation of the ellipse ends. The primary distinctions among various scenarios are observed in the zones of tensile failure. With increasing inclination angles, the areas of tensile plastic zone expand, notably smallest when the long axis aligns parallel to the maximum principal stress.

A quantitative analysis was conducted to assess the influence of

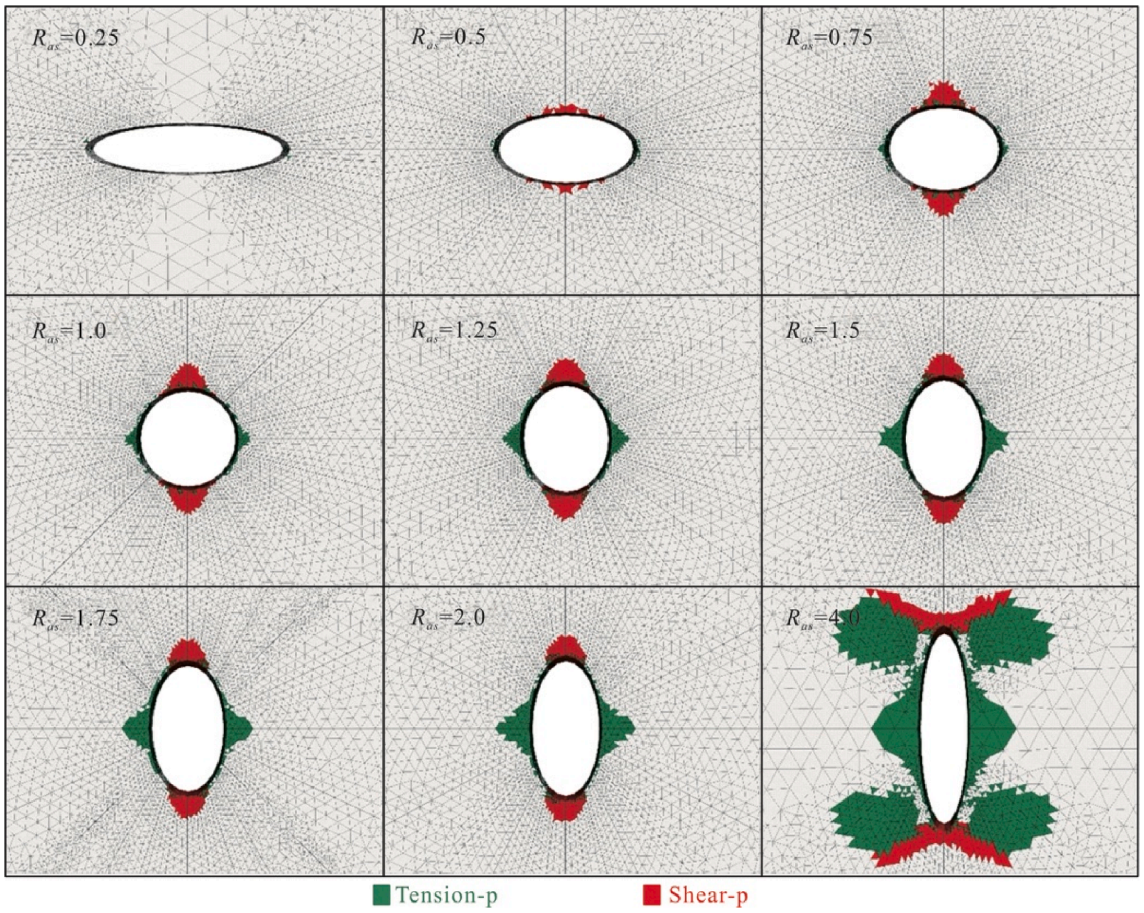

Fig. 8. Plastic zone of elliptical excavations with different aspect ratios.

Table 3
Volume of the plastic zones from rectangular and elliptical excavation.

Case	Aspect ratio	Volume of plastic zone (m^3)		
		Tensile	Shear	Total
Rectangular excavation	0.25	0.36	0.22	0.58
	0.50	0.73	0.40	1.13
	0.75	1.44	0.73	2.17
	1.00	2.26	1.25	3.51
	1.25	3.12	1.88	5.00
	1.50	4.00	2.86	6.86
	1.75	5.00	3.05	8.05
	2.00	5.97	3.25	9.22
	4.00	16.06	3.70	19.76
Elliptical excavation	0.25	0.02	0.00	0.02
	0.50	0.06	0.59	0.65
	0.75	0.22	1.60	1.82
	1.00	0.59	1.66	2.25
	1.25	1.13	1.72	2.85
	1.50	1.67	1.66	3.33
	1.75	2.18	1.63	3.81
	2.00	2.72	1.67	4.39
	4.00	26.28	6.61	32.89

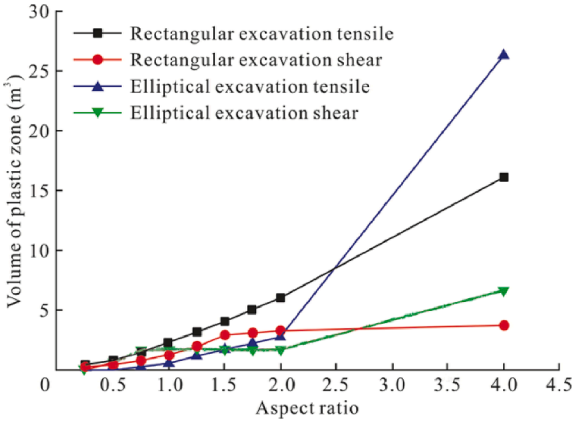

Fig. 9. Volumes of tensile and shear plastic zones in rectangular and elliptical excavations with different aspect ratios.

inclination angles on plastic failure extents based on the dissipated plastic energy observed across different aspect ratios, 1.5, 2.0, and 3.0, as depicted in Fig. 13a.

It can be found that: when the inclination angle is below 50°, excavations with larger aspect ratios exhibit a tendency to induce less dissipated plastic energy. A noticeable increase in dissipated plastic energy is evident across all aspect ratios. Their values align when the inclination angle approaches approximately 50°, suggesting minimal influence of aspect ratios on dissipated plastic energy below this threshold. However, beyond an inclination angle of 50°, dissimilar trends emerge among various aspect ratios. Under relatively smaller aspect ratios (1.5 and 2.0), the dissipated plastic energies remain nearly constant, unaffected by changes in the inclination angles. In contrast, at an aspect ratio of 3.0, the dissipated plastic energy continues to increase. This behavior is attributed to the excavation shape resembling a crack under larger aspect ratios, leading to pronounced shear stress concentration as the crack tip aligns perpendicularly to the maximum principal stress.

Fig. 13b illustrates the released kinetic energies across the aforementioned scenarios. A consistent trend of increasing energy release

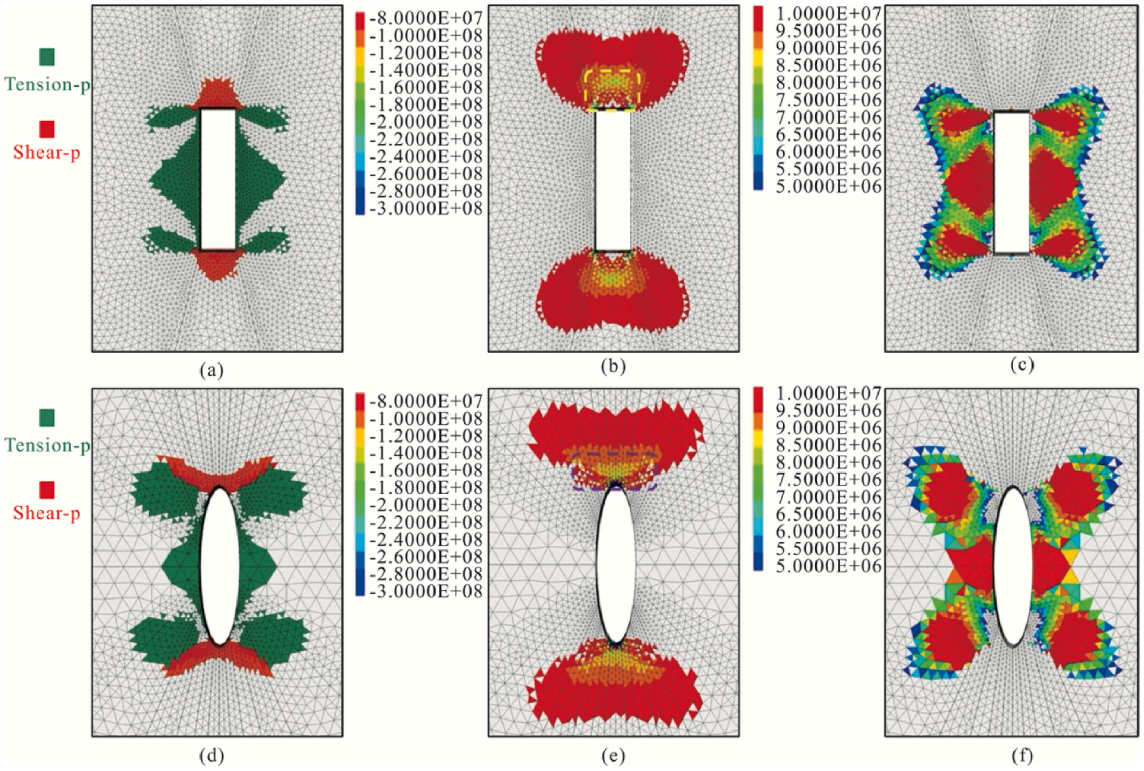

Fig. 10. Rectangular and elliptical excavation plastic zone: comparison of maximum and minimum principal stress zones when R_{as} is 4.0.

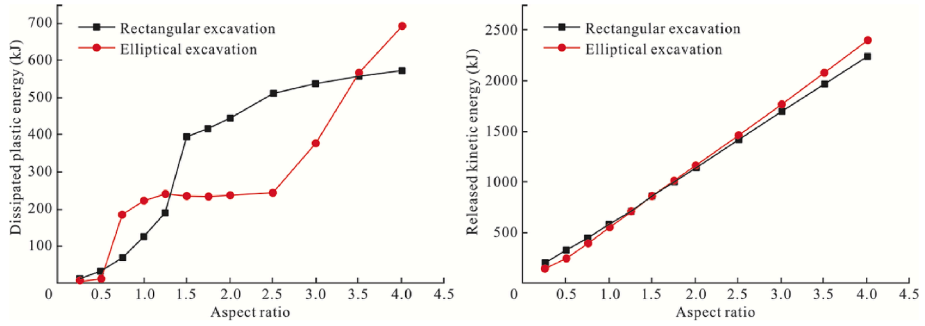

Fig. 11. Energy in rectangular and elliptical excavations with different aspect ratios.

accompanies rising inclination angles across all cases with varying aspect ratios. Specifically, at a zero-degree inclination angle, excavations with larger aspect ratios demonstrate lower released kinetic energy. Moreover, the rate of increase in kinetic energy amplifies notably with larger aspect ratios. Consequently, the curves intersect around a 20° inclination angle, signifying a very small effects of aspect ratio at this angle.

According to Fig. 13, it becomes evident that at zero inclination angle, both dissipated plastic energy and released kinetic energy are minimized. The impact of inclination angles on these energies becomes more pronounced with larger aspect ratios. Notably, critical inclination angles emerge around 50° for dissipated plastic energy and approximately 20° for released kinetic energy, wherein the influence of aspect ratios on these energies can be nearly ignored.

4.3. Effect of altered in situ stress

The anisotropy of in-situ stress also plays a crucial role in the influence of excavation aspect ratio and inclination angle. The previous analysis is based on field-measured in-situ stresses: $\sigma_1 = 60$ MPa, $\sigma_2 = 45$ MPa and $\sigma_3 = 11$ MPa. To clarify the effect of in-situ stress variations, σ_2 is kept constant at 45 MPa, while σ_3 is varied to 20 and 30 MPa. K is defined as the ratio vertical to horizontal stress:

$$K = \sigma_3 / \sigma_1 \tag{15}$$

where K is set to approximate 1/6, 1/3, and 1/2, respectively.

Fig. 14 illustrates the evolution of dissipated plastic energy and released kinetic energy with increasing aspect ratio for both elliptical and rectangular excavations. Fig. 14a–b shows the dissipated plastic energy for $K = 1/3$ and $K = 1/2$. It is observed that changes in K have limited influence on the overall trend of plastic energy dissipation for rectangular excavations but significantly reduce the peak dissipation values. For elliptical excavations, a distinct plateau appears, with dissipation stabilizing beyond an aspect ratio of 1.25. Interestingly, as K increases, the inflection point of plastic energy growth shifts from 2.5 to 3.0 to 3.5, and the growth rate slows. This is because increasing K reduces the anisotropy of the in-situ stress field, weakening stress concentration at cracks perpendicular to the maximum principal stress (as in elliptical excavations with $R_{as} = 4.0$), resulting in slower plastic energy dissipation. Fig. 14c–d displays the released kinetic energy for

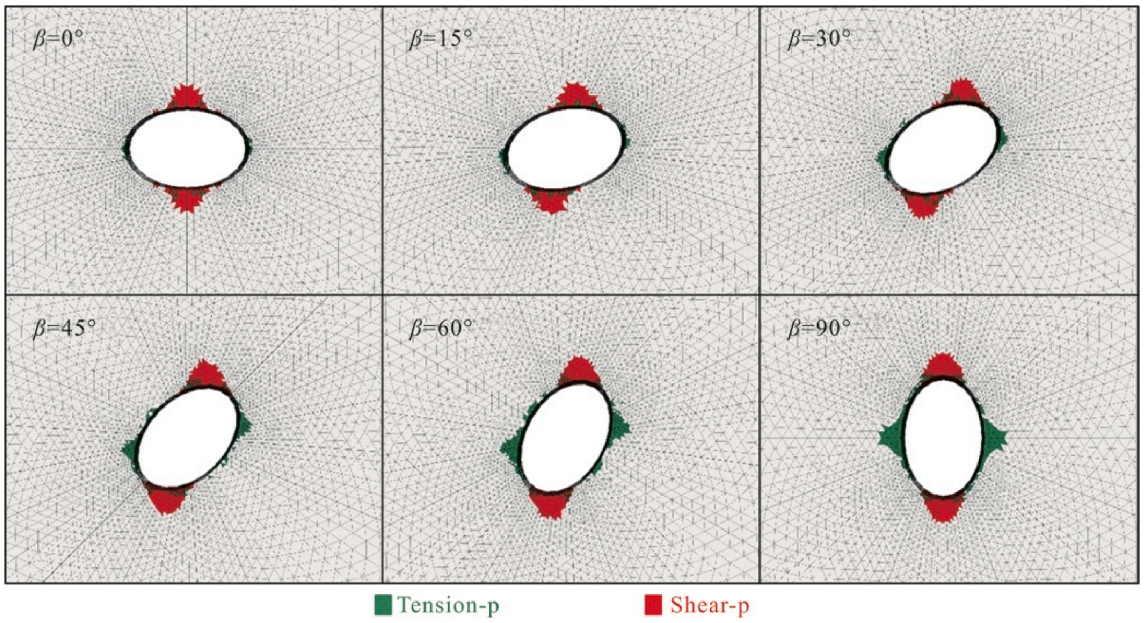

Fig. 12. Plastic zone of elliptical excavations with different inclined angles (aspect ratio = 1.5).

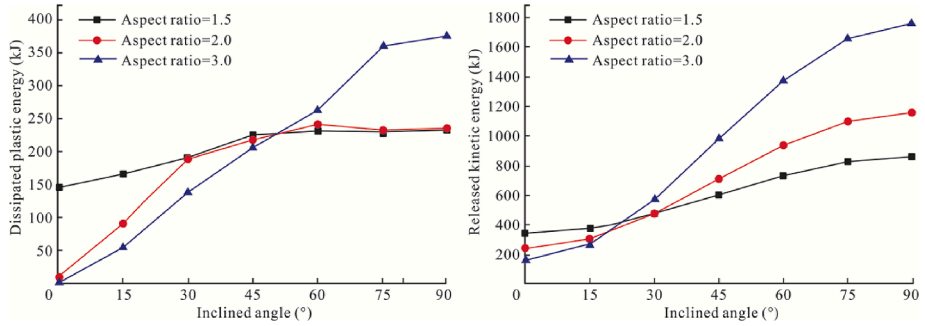

(a) Dissipated plastic energy (b) Released kinetic energy

Fig. 13. Energy in elliptical excavations with different inclined angles and aspect ratio.

$K = 1/3$ and $K = 1/2$. The impact of K on kinetic energy release is similarly limited. Overall, released kinetic energy increases with aspect ratio, consistent with the trend shown in Fig. 11b. However, the critical aspect ratio at which elliptical excavations begin to released more kinetic energy than rectangular ones shift: from 1.5 for $K \approx 1/6$ to approximately 2.0 and 2.5 for $K = 1/3$ and $1/2$, respectively. Notably, for $K = 1/2$, the released kinetic energy is the lowest at an aspect ratio of 0.5 for both excavation shapes, with the elliptical case exhibiting slightly lower values. This aligns with the findings of G. Ren et al. [41] who concluded that the optimal excavation shape occurs when the excavation aspect ratio matches the in-situ stress ratio, demonstrating the reliability of energy-based evaluation for excavation geometry.

To examine the influence of in-situ stress anisotropy on excavation inclination, a series of simulations were conducted for elliptical excavations with aspect ratios of 1.5, 2.0, and 3.0 under K values of 1/3 and 1/2, as shown in Fig. 15. Fig. 15a–b presents the dissipated plastic energy at different inclination angles for $K = 1/3$ and $K = 1/2$, respectively. Overall, the trends in plastic energy dissipation are similar across different K values. However, as K increases, the differences in dissipation among various aspect ratios become less pronounced, and the dissipation levels converge beyond a certain inclination angle. For an aspect ratio of 3.0, a significant decrease in dissipated energy is observed when the inclination angle exceeds 60°. Moreover, the critical inclination angle decreases with decreasing stress anisotropy, dropping to 45° and 30° for $K = 1/3$ and 1/2, respectively. Fig. 15c–d shows the released kinetic energy under the same conditions. For all K values, released kinetic energy increases with inclination angle across all aspect ratios. Notably, the critical inclination angle for peak kinetic energy release also decreases with increasing K: approximately 15° for $K = 1/3$ and near 0° for $K = 1/2$.

These results indicate that: while changes in the stress ratio K have a limited impact on the general trends of energy dissipation and release, they significantly affect the critical aspect ratio and inclination angle. When the excavation aspect ratio matches the in-situ stress ratio, particularly in elliptical excavations, both the dissipated plastic energy and released kinetic energy are minimized, representing an optimal excavation strategy.

5. Conclusions

The investigation of excavations' responses to varying shapes, aspect ratios, inclined angles and in-situ stress yielded intriguing insights. Examining the effects of shape, the manifestations of tensile and shear plastic zone around rectangular and elliptical excavations provided valuable observations. Tensile plastic zone in rectangular excavations notably aligned with the left and right walls perpendicular to the maximum principal stress, while shear plastic zone concentrated at

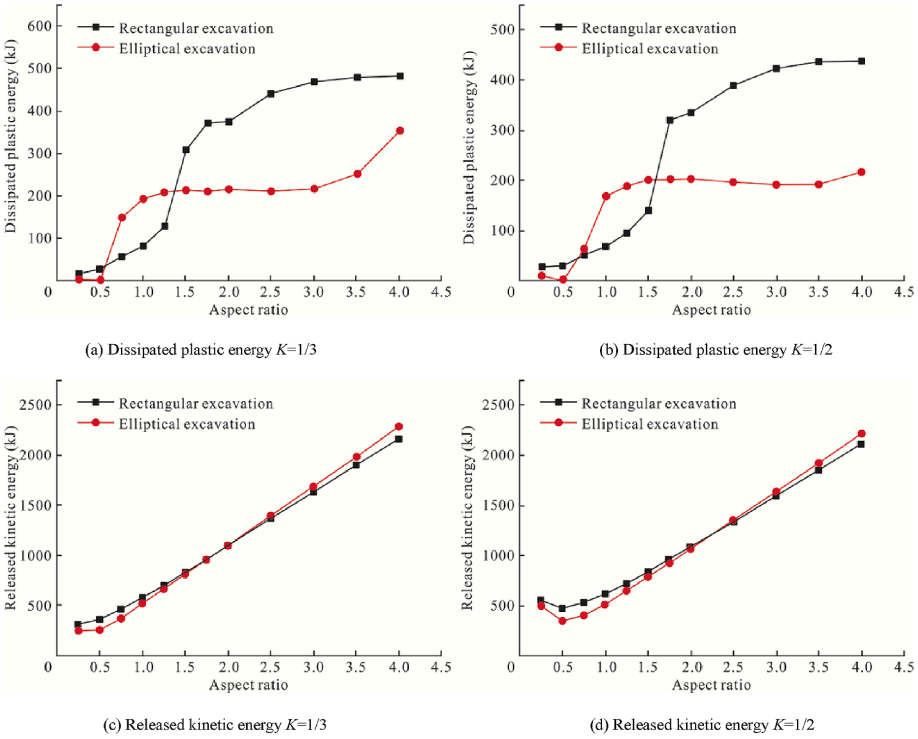

Fig. 14. Energy in rectangular and elliptical excavations with different aspect ratios.

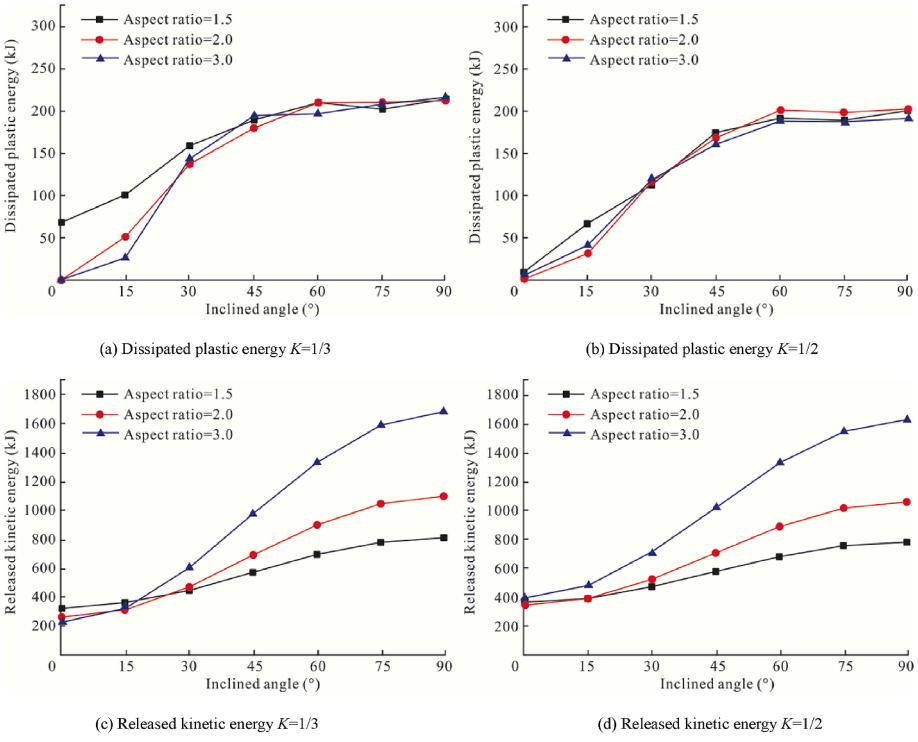

Fig. 15. Energy in elliptical excavations with different inclined angles and *K*.

corners due to compressive stress concentration. The aspect ratio played a pivotal role in determining the extent and distribution of these plastic zones, notably influencing dissipated plastic energy.

Comparing dissipated plastic energy between rectangular and elliptical excavations unveiled distinct trends. While both exhibited increasing energies with rising aspect ratios, their growth rates varied significantly. The dissipated plastic energy for elliptical excavations showcased three distinct stages, marking critical aspect ratios where drastic changes occurred. The released kinetic energy, however, displayed a linear increase across aspect ratios for both shapes, diverging from dissipated plastic energy trends. The influence of excavation shape on the evolution of released kinetic energy differs around an aspect ratio of 1.5.

Further exploration into the effects of inclined angles on plastic failure revealed compelling dynamics. Excavations with larger aspect

ratios exhibited less dissipated plastic energy at inclination angles below 50°, with notable increments across all aspect ratios as the inclination angles increased. Under the given in-situ stress conditions, critical inclination angles around 50° for dissipated plastic energy and approximately 20° for released kinetic energy, delineate points where aspect ratio effects became negligible.

Variations in the degree of in-situ stress anisotropy have a limited effect on the overall trends of dissipated plastic energy and released kinetic energy, but they significantly alter the critical aspect ratio and inclination angle. When the in-situ stress ratio matches the excavation aspect ratio, both forms of energy reach their minimum values.

These findings highlight the intricate interplay between excavation shapes, aspect ratios, and inclined angles concerning plastic and kinetic energies. They underscore the necessity of a nuanced approach when optimizing excavation designs, acknowledging the distinct impacts of shape, aspect ratio, inclination angles and in-situ stress on failure mechanisms and energy dissipation. Ultimately, achieving optimal excavation designs demands a holistic consideration of these multifaceted factors to mitigate failure and manage induced dynamic disturbances effectively.

CRediT authorship contribution statement

Linnea Lundvall: Validation, Writing – original draft, Formal analysis. **Niklas Burvall:** Writing – original draft, Investigation, Software. **Zongze Li:** Investigation, Writing – review & editing, Funding acquisition. **Wenjun Luo:** Validation, Data curation, Methodology. **Jinyang Fan:** Investigation, Writing – review & editing, Formal analysis. **Minghe Ju:** Validation, Data curation, Methodology. **Yang Zou:** Supervision, Writing – original draft, Funding acquisition.

Declaration of competing interest

All authors declare that they have no known competing financial interests or personal relationships that could have appeared to influence the work reported in this paper.

Acknowledgements

This work was supported by the Opening Research Fund of State Key Laboratory of Coal Mine Disaster Dynamics and Control in China (No. 2011DA105287-FW202409), State Key Laboratory of Intelligent Construction and Healthy Operation and Maintenance of Deep Underground Engineering in China (No. SDGZ2503). The authors are also grateful for the financial support from the Rut and Sten Brand foundation.

References

[1] M. Askaripour, A. Saeidi, A. Rouleau, P. Mercier-Langevin, Rockburst in underground excavations: a review of mechanism, classification, and prediction methods, Undergr. Space 7 (2022) 577–607.
[2] B.P. Simser, Rockburst management in Canadian hard rock mines, J. Rock Mech. Geotech. Eng. 11 (2019) 1036–1043.
[3] Y. Fanjie, Z. Hui, X. Haibin, M.U. Azhar, Z. Yong, C. Fudong, Numerical simulation method for the process of rockburst, Eng. Geol. 306 (2022) 106760.
[4] P. Małkowski, Z. Niedbalski, A comprehensive geomechanical method for the assessment of rockburst hazards in underground mining, Int. J. Min. Sci. Technol. 30 (2020) 345–355.
[5] M. Zhang, J. Zhang, J. Fan, Z. Li, J. Chen, Y. Zou, D. Jiang, D. Nelias, Model interpretability and intensity prediction of rockbursts using a method innovation based on the QGHSCSO-CatBoost algorithm, Rock Mech. Rock Eng. 30 (2025) 1–30.
[6] A. Mazaira, P. Konicek, Intense rockburst impacts in deep underground construction and their prevention, Can. Geotech. J. 52 (10) (2015) 1426–1439.
[7] M. He, Q. Wang, Rock dynamics in deep mining, Int. J. Min. Sci. Technol. 33 (2023) 1065–1082.
[8] J. Fan, J. Chen, D. Jiang, J. Wu, C. Shu, W. Liu, A stress model reflecting the effect of the friction angle on rockbursts in coal mines, Geomech. Eng. 18 (2019) 21–27.
[9] Y. Pan, A. Wang, Disturbance response instability theory of rock bursts in coal mines and its application, Geohazard Mech 1 (1) (2023) 1–17.
[10] N.L.L. Mambou, J. Ndop, J.-M.B. Ndjaka, Redistribution and magnitude of stresses around horse shoe and circular excavations opened in anisotropic rock, Int. J. Min. Sci. Technol. 25 (4) (2015) 615–621.
[11] F. Yang, Z. Li, M. Fourmeau, J. Fan, Z. Yang, D. Jiang, Daniel Nelias, A unified constitutive model for salt rocks under triaxial creep-fatigue loading conditions, Tunn. Undergr. Space Technol. 154 (2024) 106116.
[12] Y. Hu, Z. Sun, J. Ji, Pseudo-dynamic stability analysis of 3D rock slopes considering tensile strength-modified Hoek–Brown failure criterion: seismic UBLA implementations, Eng. Geol. 343 (2024) 107786.
[13] J.H. Yang, C. Yao, Q.H. Jiang, W.B. Lu, S.H. Jiang, 2D numerical analysis of rock damage induced by dynamic in-situ stress redistribution and blast loading in underground blasting excavation, Tunn. Undergr. Space Technol. 70 (2017) 221–232.
[14] H.A. Elsageer, S.D. Butt, A.O. Mohammad Bamousa, W.R.E. Abdellah, M.A.M. Ali, Distribution of Stress Around Underground Excavations. Essentials Rock Mech, Springer, 2024, pp. 173–213.
[15] M.D.G. Salamon, Energy considerations in rock mechanics: fundamental results, J South African Inst Min Metall 84 (8) (1984) 233–246.
[16] E.T. Brown, J.W. Bray, F.J. Santarelli, Influence of stress-dependent elastic moduli on stresses and strains around axisymmetric boreholes, Rock Mech. Rock Eng. 22 (3) (1989) 189–203.
[17] R. Zhao, M. Tao, H. Zhao, C. Wu, W. Cao, Theoretical study on dynamic stress redistribution around circular tunnel with different unloading paths, Comput. Geotech. 163 (2023) 105737.
[18] Z. Li, J. Fan, M. Fourmeau, J. Chen, D. Jiang, D. Nelias, Long-term deformation of rock salt under creep–fatigue stress loading paths: modeling and prediction, Int. J. Rock Mech. Min. Sci. 181 (2024) 105861.
[19] Z.Y. Ai, Q. Liang, Z.K. Ye, K.X. Hu, Stress distribution around arbitrarily shaped shallow buried tunnels in transversely isotropic rock mass, Int. J. Numer. Anal. Methods GeoMech. 49 (5) (2025) 1378–1395.
[20] K. Duan, C.Y. Kwok, Evolution of stress-induced borehole breakout in inherently anisotropic rock: insights from discrete element modeling, J. Geophys. Res. Solid Earth 121 (4) (2016) 2361–2381.
[21] R. Gu, U. Ozbay, Numerical investigation of unstable rock failure in underground mining condition, Comput. Geotech. 63 (2015) 171–182.
[22] H. Xie, C. Li, Z. He, C. Li, Y. Lu, R. Zhang, et al., Experimental study on rock mechanical behavior retaining the in situ geological conditions at different depths, Int. J. Rock Mech. Min. Sci. 138 (2021) 104548.
[23] Y. Zou, W. Sharief, Z. Li, J. Fan, D. Jiang, D. Nelias, Numerical assessment of the influence of residual rock mass properties on destress blasting in deep mine, Earth Energy Sci. 1 (4) (2025) 324–335.
[24] L. Jing, J.A. Hudson, Numerical methods in rock mechanics, Int. J. Rock Mech. Min. Sci. 39 (4) (2002) 409–427.
[25] Y. Zou, P. Zhang, Assessment of Energy Release and Redistribution on Excavation Instabilities for Underground Mining, ISRM Congr., ISRM, 2023. ISRM-15CONGRESS.
[26] E. Eberhardt, Numerical modelling of three-dimension stress rotation ahead of an advancing tunnel face, Int. J. Rock Mech. Min. Sci. 38 (4) (2001) 499–518.
[27] F. Wang, R. Kaunda, Assessment of rockburst hazard by quantifying the consequence with plastic strain work and released energy in numerical models, Int. J. Min. Sci. Technol. 29 (1) (2019) 93–97.
[28] J. Watson, I. Canbulat, C. Zhang, C. Wei, Energies within rock mass and the associated dynamic rock failures, Rock Mech. Rock Eng. 58 (5) (2025) 4935–4958.
[29] I. Vazaios, M.S. Diederichs, N. Vlachopoulos, Assessment of strain bursting in deep tunnelling by using the finite-discrete element method, J. Rock Mech. Geotech. Eng. 11 (1) (2019) 12–37.
[30] J. Zhou, Y. Zhang, C. Li, H. He, X. Li, Rockburst prediction and prevention in underground space excavation, Undergr. Space 14 (2024) 70–98.
[31] S.-J. Miao, M.-F. Cai, Q.-F. Guo, Z.-J. Huang, Rock burst prediction based on in-situ stress and energy accumulation theory, Int. J. Rock Mech. Min. Sci. 83 (2016) 86–94.
[32] J.A. Hudson, J.P. Harrison, Engineering Rock Mechanics: an Introduction to the Principles, Elsevier, 2000.
[33] Szwedzicki Tad, The effect of mining geometry on stability of rock mass around underground excavations, Miner. Resour. Eng. 9 (2) (2000) 265–278.
[34] G. Ren, Z.H. Zuo, Y.M. Xie, J.V. Smith, Underground excavation shape optimization considering material nonlinearities, Comput. Geotech. 58 (2014) 81–87.
[35] L.-T. Xie, P. Yan, W.-B. Lu, M. Chen, G.-H. Wang, Effects of strain energy adjustment: a case study of rock failure modes during deep tunnel excavation with different methods, KSCE J. Civ. Eng. 22 (10) (2018) 4143–4154.
[36] H. Liu, Z. An, X. Liu, X. Wang, Z. Liu, An experimental investigation on the characteristics of excavation-induced failure of rocks surrounding a shaft, Adv. Civ. Eng. 2024 (1) (2024) 7363711.
[37] J.B. Martino, N.A. Chandler, Excavation-induced damage studies at the underground research laboratory, Int. J. Rock Mech. Min. Sci. 41 (8) (2004) 1413–1426.
[38] X. Dong, A. Karrech, H. Basarir, M. Elchalakani, A. Seibi, Energy dissipation and storage in underground mining operations, Rock Mech. Rock Eng. 52 (1) (2019) 229–245.
[39] V. Hajiabdolmajid, P.K. Kaiser, C.D. Martin, Modelling brittle failure of rock, Int. J. Rock Mech. Min. Sci. 39 (6) (2002) 731–741, https://doi.org/10.1016/S1365-1609(02)00051-5.
[40] R.S. Read, 20 years of excavation response studies at AECL's underground research laboratory, Int. J. Rock Mech. Min. Sci. 41 (8) (2004) 1251–1275.
[41] G. Ren, J.V. Smith, J.W. Tang, Y.-M. Xie, Underground excavation shape optimization using an evolutionary procedure, Comput. Geotech. 32 (2) (2005) 122–132.